MOTION CORRECTION OPTIONS IN PET/MRI

Ciprian Catana, MD, Ph.D.

Athinoula A. Martinos Center for Biomedical Imaging, Department of Radiology, Massachusetts General Hospital, Assistant Professor in Radiology, Harvard Medical School, Mailing address: 149, 13th St. Room 1116, Charlestown, MA 02129, Tel: +1-617-643-4885, Fax: +1-617-726-7422

Ciprian Catana: ccatana@nmr.mgh.harvard.edu

Abstract

Subject motion is unavoidable in clinical and research imaging studies. Breathing is the most important source of motion in whole-body positron emission tomography (PET) and magnetic resonance imaging (MRI) studies, affecting not only thoracic organs but also those in the upper and even lower abdomen. The motion related to the pumping action of the heart is obviously relevant in high-resolution cardiac studies. These two sources of motion are periodic and predictable, at least to a first approximation, which means certain techniques can be used to control the motion (e.g. by acquiring the data when the organ of interest is relatively at rest). Additionally, non-periodic and unpredictable motion can also occur during the scan. One obvious limitation of methods relying on external devices (e.g. respiratory bellows or the ECG signal to monitor the respiratory or cardiac cycle, respectively) to trigger or gate the data acquisition is that the complex motion of internal organs cannot be fully characterized. However, detailed information can be obtained either using the PET or MRI data (or both) allowing the more complete characterization of the motion field so that a motion model can be built. Such a model and the information derived from simple external devices can be used to minimize the effects of motion on the collected data. In the ideal case, all the events recorded during the PET scan would be used to generate a motion free/corrected PET image. The detailed motion field can be used for this purpose by applying it to the PET data before, during or after the image reconstruction. Integrating all these methods for motion control, characterization and correction into a workflow that can be used for routine clinical studies is challenging but could potentially be extremely valuable given the improvement in image quality and reduction of motion-related image artifacts.

INTRODUCTION

Positron emission tomography (PET) and magnetic resonance imaging (MRI) are both powerful imaging modalities widely used for oncologic and cardiac research and clinical imaging studies. With a spatial resolution on the order of a few millimeters full-width-at-half-maximum for state-of-the-art PET scanners and in the submillimeter range for MRI, even small amplitude motion can have a substantial effect on the acquired data. In PET studies, motion makes difficult the detection of small lesions, the accurate quantification of tracer uptake in therapy monitoring studies, the precise definition of the tumor volume for radiotherapy and surgical planning. Furthermore, the mismatch between the attenuation and emission data when the two are acquired sequentially, leads to inaccurate quantification and image artifacts. In the case of MRI, even small amplitude motion can severely blur the

images or introduce artifacts due to incorrect sampling of the data in the Fourier domain (k-space).

Numerous methods have been proposed for controlling the respiratory or cardiac motion or minimizing its effects. More interestingly, methods to characterize and compensate for this motion have been developed. The algorithms proposed for motion compensation can be broadly classified in three classes based on the way the motion information is used for generating the motion-corrected PET images (i.e. pre-, during or post-reconstruction). Each class of methods has its own advantages and disadvantages and is more suitable for certain applications (1).

Recently, integrated whole-body PET/MRI scanners capable of simultaneous data acquisition have been introduced (2, 3) and proof-of-principle studies in various patient populations have been performed (Figure 1). There is great excitement about the potential research and clinical applications of this novel imaging modality (4) but motion needs to be addressed before PET/MR can reach its full potential. This is not only a challenge but also a great opportunity from a methodological perspective, as improved motion correction in PET/MRI scanners could be a game-changer much the same way CT-based attenuation correction has proven to be in the PET/CT field (5, 6).

MOTION IN WHOLE-BODY IMAGING STUDIES: SOURCES AND MAGNITUDE

Respiratory motion

In inspiration, the contraction of the intercostal muscles and diaphragm leads to the expansion of the thoracic space and a decrease in the intrathoracic pressure. As a result, the lungs expand and fill with air. In expiration, the muscles relax and the air is expelled from the lungs. Early studies have suggested that the diaphragmatic contribution to the respiration is three times that of the rib cage muscles but there is a lot of variability between subjects and even between breathing cycles for the same individual (7). Although respiration can be assumed to be periodic, the path along which the various organs travel during inspiration is different than the one followed in expiration, a phenomenon termed hysteresis. The amplitude of the motion also depends on the type of respiration. During normal breathing, the diaphragm moves 1.5 cm and the chest circumference changes 0.7 cm in the supine position, while the range of values following a deep inspiration is 7–13 cm and 5–11 cm, respectively (7).

The effect of breathing on the motion of lung tumors was investigated in the context of radiotherapy planning by analyzing the displacements of the gross tumor volumes delineated from the CT images acquired in different parts of the respiratory cycle (8) or from respiration-correlated CT data (9). The mean displacements observed were 1, 0.9 and 0.8 cm in the cranio-caudal, anterior-posterior and lateral directions, respectively. More importantly, significant intra-patient variability was observed (8).

Interestingly, even the heart moves rigidly with the respiration (in addition to the more complex motion due to the cardiac contraction discussed in the next section), the ranges

reported were from 3.8 to 23.5 mm, −1.3 to 11.5 mm and −1.8 to 6.1 mm in the cranio-caudal, anterior-posterior and right-left direction, respectively (10). Similar values and a predominantly cranio-caudal respiration-induced motion correlated to the motion of the diaphragm in the same direction were also reported in other studies (11). In this context, it is worth mentioning the more complicated impact of respiration on heart motion, the heart rate and motion being different in the two parts of the respiratory cycle (12). Furthermore, the breath hold techniques routinely used for PET and MRI data acquisition lead to changes in the heart rate (13).

Studies aimed at investigating the motion of the liver secondary to respiration have predominantly reported cranio-caudal translations ranging from 10 to 26 mm in normal inspiration and up to 75 mm in deep inspiration (14–16). Subsequent studies (mostly performed using MRI) revealed up to 10 mm translations in the anterior-posterior and lateral directions (17). A more advanced study also demonstrated non-rigid transformations (i.e. deformations) of the liver on the order of 10 mm averaged across the whole liver (18).

Although the displacement of the spleen was not routinely analyzed or reported in many studies, it appears to be quite variable between subjects and on the order of 2 cm in the cranio-caudal direction, 1 cm in the anterior-posterior direction and 5 mm in the lateral direction (19).

The motion of tumors in the pancreas was studied using cine MRI (20) or volumetric cine CT (21). The range of motion in the cranio-caudal direction was 13–42 mm, while in the anterior-posterior direction was 3–13 mm. Non-rigid deformation of the pancreas with respiration was also observed. The motion of neither the diaphragm or the abdominal wall was correlated with the motion of the pancreatic tumor borders, suggesting these are not adequate surrogates for monitoring the motion (20).

The translations of the kidney as assessed from 4D CT data by the displacement of the center of gravity of the organ ranged from 2.5 to 20.5 mm, 0.6 to 8 mm and 0.4 to 5.9 mm in the cranio-caudal, anterior-posterior and lateral directions (22). While similar mean displacements on the order of 7.4 mm were reported for the left and right kidneys, the amplitude of the liver dome or abdominal wall motion, which are sometimes used as motion surrogates, was correlated only with the right kidney displacement. Only the abdominal motion of the diaphragm was moderately correlated with that of the kidney (23). However, even this potential surrogate was demonstrated to be unreliable in predicting the kidney position in pediatric patients (24). Interestingly, the same study demonstrated that the amount of motion in the cranio-caudal direction increases with age, while the motion in the lateral direction increases with height.

A true fast imaging with steady-state precession (TrueFISP) MR sequence was used to acquire dynamic imaging of the prostate at 3 frames/second for several breathing cycles in healthy volunteers and patients with adenocarcinoma of the prostate (25). In approximately a third of the patients, the motion of the prostate was assessed with and without an endorectal coil present for the MR examination. While the range of the movement of the base of the prostate was 0.5 to 10.6 mm and 0.3 to 10 mm in the cranio-caudal and anterior-posterior

direction, respectively, in 69% of the patients the displacement of the prostate was smaller than 3 mm. Not surprisingly, the presence of the endorectal coil significantly reduced the displacements in both directions. No statistically significant differences in prostate motion were observed between healthy volunteers and patients, although it was noted that this finding might depend on the stage of the disease.

One aspect that should be emphasized is that the motion path of abdominal organs is also different in the two parts of the respiratory cycle (19).

Cardiac motion

Motion of the cardiac ventricles throughout the cardiac cycle is very complex, involving longitudinal and radial contractions, as well as rotations of the apex and the base in opposing directions (26). The directions and magnitudes of these displacements for the left ventricle not only vary from the base to the apex (i.e. longitudinally), but also for the different walls (i.e. circumferentially), as well as from the epicardium to the endocardium (i.e. radially). For example, the mean maximal displacement was 11.2 mm for the base, 6.9 mm for the midpoint and only 2.6 mm for the apex (27) of the ventricle. The mean radial strain (reflecting wall thickening in systole) was approximately 30% (translating in ~5 mm inward displacement), while the mean circumferential strain was −21% for the base and −25.3% for the apex (negative strains represent segment shortening). A 16.8% variation between the mean maximal circumferential strains measured in the epicardium and endocardium was reported (27).

While cardiac motion does not have a significant influence on abdominal organs, its impact on the adjacent organs is not negligible. For example, lateral motion on the order of 1 to 4 mm was observed in lung tumors, particularly those located close to the heart (28). A maximum displacement of the esophagus in the transverse direction of 10 mm due to cardiac motion was also reported. This displacement was also dependent on the phase of the cardiac cycle and varied in the cranio-caudal direction (29). The region of the liver adjacent to the heart is displaced by approximately 4 mm in normal controls. Interestingly, this value is actually smaller in cirrhotic patients due to the higher stiffness of the liver (30).

Other sources of motion

There are other sources of motion that are more localized in terms of their effect but are relevant in specific studies. For example, the impact of deglutition (swallowing) has been studied using MRI in head-and-neck cancer patients. The gross tumor volume was displaced up to 13.7, 12, 28.4 and 19.4 mm in the anterior, posterior, superior and inferior direction, respectively. Significant displacements were observed in several other structures, such as the soft palate, vocal cord and epiglottis. Intersubject variability in terms of frequency and duration of deglutition was also reported (31).

Peristalsis is known to reduce the quality of abdominal imaging exams and often bowel relaxants are administered to minimize its effects. The rectum can distend due to accumulation of air and fecal material during the imaging session and this could have an impact on the position of adjacent organs. For example, a 4.2 mm mean displacement of the prostate in the anterior-posterior direction due to this source of motion was reported (32).

Similar amplitude drifts of the prostate in the posterior and inferior directions were observed in a different study and were attributed to gradual bowel movements or relaxation of the pelvic musculature (33). Clenching of the pelvic muscles has also been discussed as a source of intermittent prostate motion (32). The position of the prostate could also be affected by the degree of filling of the bladder. Although clear instructions are given to the subjects to void before the imaging exam, the bladder can refill during long studies. It was actually shown that the dimensions of the bladder change by 2.1, 1.1 and 1.6 cm in the cranio-caudal, anterior-posterior and lateral directions, respectively (34).

Coughing leads to a contraction of the abdominal wall muscles. For example, the range of motion of the prostate due to coughing was 0.6 to 27 mm and 0.7 to 26 mm in the cranio-caudal and anterior-posterior directions, respectively, values that were significantly larger than those observed during normal respiration in the same group of subjects (25).

In addition to all these "physiological" and largely unavoidable sources for motion, patients often adjust their position in the scanner voluntarily or involuntarily which leads to bulk motion and unpredictable and non-periodic displacements and deformations of the internal organs. Patient preparation, padding to restrict the motion, sedation/anesthesia in pediatric patients are used to minimize these sources of motion (35).

TECHNIQUES TO CONTROL MOTION OR MINIMIZE ITS EFFECTS

Respiratory motion

Gating techniques have been proposed to minimize the effects of respiratory motion on the PET images by dividing the emission data in short duration bins corresponding to the various parts of the respiratory cycle. This is accomplished using an external device to obtain the respiratory signal, which is used as a surrogate for internal organ motion. A motion model relates this respiratory signal to the displacement of the organs of interest (36). During the imaging study, the respiratory signal is recorded and synchronized with the PET data acquisition. Various external devices are currently used for respiratory gating in PET studies performed using stand-alone or PET/CT scanners (37). For example, a pressure sensor mounted in a chest belt can be used to monitor the changes related to the displacement of the thoracic cage. Alternatively, optical based methods can be used track the position of reflective markers placed on the subject's thorax. More involved methods include the monitoring of the changes in temperature of the air in the upper airways changes or of the volumes of air inhaled and exhaled during respiration (38). Methods to derive the same information directly from the emission data have also been proposed (39–42). For example, in one of these approaches, a dynamic series of sinograms of 100 ms duration were generated from the list mode data. The regions in the sinogram space that were affected by motion were selected using spectral analysis to generate a mask. The respiratory signal was estimated from the plot of the summed counts in the mask versus time and was shown to correlate very well with that obtained using the optical-based approach (41).

Once the respiratory signal is available, the respiratory cycle can be divided into several bins either as a function of time or amplitude and the emission data corresponding to these bins can be presented in a histogram (43). A larger number of bins would lead to a minimization

of the motion effects. However, this would also mean shorter duration gates and hence a decrease in the signal-to-noise ratio (SNR) in the resulting images. An additional factor that has to be considered is that only one attenuation map is usually available. Since this map might be obtained in a position that does not match any of the bins, an attenuation-emission mismatch could be present, leading to artifacts in the resulting images. To minimize this effect in PET/CT imaging and given the fact that the diagnostic CT is usually performed at end-inspiration, a deep-inspiration breath-hold protocol was proposed (44). As the name suggests, the emission data in this case are collected over several end-inspiration breath holds, with the patient relaxing between these acquisitions. Various other techniques have been proposed for reducing the respiration-induced emission-attenuation mismatch in PET/CT imaging but they will not be further discussed here given the different nature of the MR data acquisition compared to CT.

Breath holding can also be used to minimize the effect of motion in MRI studies. As opposed to PET, one segment of the k-space is sampled during each breath hold until all the data are acquired. This requires patient compliance to "freeze" the motion in the same position between successive breath holds. Even in this case, it was shown that the diaphragm can drift substantially at the end of long breath holds (45). Interestingly, the displacements during an end-expiration breath hold were smaller (2.6 versus 29.9 mm) than after a deep inspiration, which is the preferred method for thoracic CT studies.

To avoid these limitations, the respiratory signal can be derived from surrogate data under the assumption that these data are correlated with the actual motion of the organ of interest. The respiratory bellows or optical devices discussed in the previous section can be used for deriving the respiratory signal. Alternatively, navigator pulses derived directly from the MRI data could track the cranio-caudal motion of the right hemi-diaphragm (46). These very short acquisitions can be performed right before the imaging data are acquired and allow the monitoring of the displacement of the lung-liver interface. If the position is in the desired range, the data are acquired; otherwise the corresponding k-space segment is reacquired. In an approach termed slice tracking, the estimated displacement can be used to adjust the position of the imaging volume in a prospective manner (47). The surrogate data can be obtained using even higher dimensional data (36). Furthermore, these advanced navigators can be used to test the validity of the motion model (48).

Motion can be derived directly from the MR data without the need for navigators, an approached called self-navigation (49). These techniques require that the k-space be sampled in a motion-insensitive manner (e.g. radially or spirally). The free-breathing motion can be detected by repeatedly acquiring a central profile in k-space and comparing each projection to a reference position obtained in the "learning" stage. This is performed in real-time so that the motion-corrupted data (i.e. k-space segment) can be reacquired (49).

Cardiac motion

The cardiac cycle can also be divided into short frames (e.g. 50–100 ms) to minimize the effect of the motion related to the cardiac activity and the ECG signal has proven very reliable for this purpose. If the PET data are acquired in list mode format, images corresponding to each of the bins can be reconstructed. Alternatively, the real-time detection

of certain features of the ECG signal (usually the R-wave that precedes the ventricular contraction) allows the triggering of the acquisition only in a certain part of the cardiac cycle when the heart is almost at rest. Although the motion effects can be greatly reduced using these approaches, the SNR in the resulting images is very low due the fact that most of the data are discarded.

Given the high-resolution capabilities of MRI, it is essential to minimize the motion in cardiovascular studies. Although numerous techniques have been proposed for this purpose (12), the ECG-based gating is the most widely used. Similar to respiratory gating, ECG gating can be performed prospectively or retrospectively. In the former case, the data are acquired over multiple cardiac cycles but only a segment of the k-space is sampled during each cycle after a certain delay after the R-wave. In the latter case, images acquired continuously are time-stamped so that they can be retrospectively binned (50).

Arrhythmia-rejecting algorithms can be used to minimize the effects of heart rate variability on coronary MR angiography (51, 52). Another aspect that has to be considered in the case of MRI is that the ECG signal can be corrupted by radio-frequency interference with the MR's components (i.e. transmit/receive and gradient coils). Even the static magnetic field can change the amplitude of the R-wave, a phenomenon termed magneto-hydrodynamic effect (53). To minimize these effect, advanced algorithms for the detection of the R-wave have been suggested (54).

The MR data can also be used to obtain a cardiac signal, an approach called cardiac self-gating (55, 56). Similar to the detection of the respiratory signal, an ECG-like signal is obtained from a profile of the k-space repeatedly acquired. The obvious advantage of this method is that it eliminates the need for placing ECG leads.

Combined respiratory and cardiac motion

In cardiac studies, it is critical to minimize both respiratory- and cardiac-related motion. Dual-gating was recently demonstrated in a PET/CT scanner using the real-time positioning system (RTM, Anzai) and an ECG device to send respiratory and cardiac triggers to the list-mode data. Dividing the PET data into four cardiac bins and eight respiratory amplitude bins provided the best results (57).

Real-time respiratory self-gating combined with ECG-gating has been proposed for three-dimensional cine-MRI (49). Even more advanced methods that allow the non-linear correction of the breathing-related motion seem to be required for imaging the small coronary arteries using magnetic resonance angiography (58).

One disadvantage of these methods is that separate devices are used for respiratory and cardiac gating, which increases the technical complexity and limits the clinical usefulness. As an alternative, it was shown that the ECG leads could also be used to derive a respiratory signal using bioimpedance measurements and the feasibility of performing dual-gating using this method in clinical cardiac PET studies has recently been demonstrated (59). A self-gated approach that eliminates the need for ECG-gating or breath holding in cine cardiac MR studies has been demonstrated. This method uses periodically rotated overlapping

parallel lines with enhanced reconstruction (PROPELLER) encoding (60) and post-processing to rearrange the k-space data into groups corresponding to the respiratory and cardiac phases (61).

MOTION CHARACTERIZATION

PET data driven approaches

Optical flow algorithms have been proposed for deriving the motion field directly from the PET images. Similar to gated studies, the respiratory cycle is first divided into multiple short frames and the corresponding PET images are reconstructed from these data. Next, the transformations between these images have to be estimated. For this purpose, the assumption in optical flow methods is that the voxel brightness does not change between frames close in time, meaning there is a correspondence between the voxels in those volumes. Specifically, the pixel intensity after motion depends on the velocity (optical flow) in each direction and the change in pixel intensity in the corresponding directions. The other required assumption is that the motion of adjacent voxels of the same type is smooth. To overcome the limitations of the early approaches (low density flow vectors and smoothness across boundaries), a combined local-global optical flow energy function (dependent on the image gradient and the smoothing constraint) minimized using a nonquadratic approach was proposed (62). To preserve discontinuities across organ boundaries, a weighting function was used to reduce the effect of the smoothing at the edges of the organs.

Similar methods have been used for estimating the motion of the left ventricle during the cardiac cycle (63–65). The additional challenge in this case is that the assumptions mentioned above are not correct for the voxels corresponding to the blood pool, which are adjacent to those from the left ventricle. A variable smoothness weighting which does not penalize motion discontinuities in regions with high image gradients (such as at the border between the myocardium and the chamber) has been proposed (63). In this early study, the authors acknowledged the difficulty in estimating the complex motion of the heart given the limited spatial resolution of the PET scanner and the lack of visible structures that could be tracked in the myocardium.

Another factor that complicates the motion estimation problem in this case is the partial volume effects that affect the accurate quantification in PET, being mainly dependent on the size of the structure of interest. However, the thickness of the myocardium changes significantly during the cardiac cycle, which means the ability of the PET scanner to resolve the actual uptake is better in systole than in diastole. Since this violates the brightness consistency assumption mentioned above, an alternative method relying on the conservation of mass assumption has recently been proposed (66) and relies on the fact that the total activity in organs does not change between gates (i.e. the activity is just redistributed even in the presence of partial volume effects).

Another class of algorithms that was proposed for deriving the deformation field between the gated PET images and the reference position uses B-spline deformable registration (67, 68). The local smoothness in this case was imposed by assuming the deformation field follows a Markov random field (67).

MR-based approaches

Progress with motion compensation in PET/CT has been hampered by the increased radiation exposure and the assumption that the resulting PET and CT phases match in spite of the sequential acquisition. As a consequence, the focus in PET/CT has been on motion control rather than motion characterization and compensation. However, MR does not involve ionizing radiation and the MR and PET data can now be acquired simultaneously. Numerous techniques have been proposed for characterizing the motion using MRI (12, 35).

In the simplest approach, the respiration model can be constructed from a series of 2D images repeatedly acquired over several respiratory cycles (69). The sagitally oriented images acquired using a 2-D multi-slice gradient-echo sequence are used to generate a series of 3-D volumes corresponding to the different points during the respiratory cycle. The workflow for simultaneous PET/MRI data acquisition, MR-based motion estimation using this approach and PET motion correction is summarized in Figure 2. Alternatively, respiratory-gated MR volumes can be acquired using a 3-D radial stack-of-stars spoiled gradient echo sequences (70). The motion fields can be generated from these volumes using a non-rigid registration algorithm.

More advanced MR techniques such as tagged MRI, phase contrast MRI and pulse field gradient methods can also be used to estimate the non-linear motion of internal organs (71). In this section, several of these approaches will be discussed, mainly focusing on those that have been proposed in the context of PET/MRI.

In MRI tagging techniques, the tissue of interest is "labeled" using a selective radio-frequency pulse (72) or through the spatial modulation of the magnetization (SPAMM) (73) or using a train of RF pulses as in the delay alternating with nutation for tailored excitation (DANTE) sequence (74). In an image acquired before the full recovery of longitudinal magnetization, there will be a difference in signal intensity between the tagged and untagged voxels. A certain pattern (e.g. parallel bands or a grid) is superimposed on the tissue of interest and the choice of the MR sequence parameters (i.e. flip angle, direction, strength and amplitude of the warping gradient, etc.) controls the shape, orientation and spacing between these tagging bands (73). They act like virtual fiducial markers and the deformation of the pattern is dependent on the motion of the underlying tissue. One disadvantage of these techniques is that the tagging contrast fades due to longitudinal magnetization relaxation. A complementary SPAMM (CSPAMM) sequence addresses this limitation by increasing the flip angle throughout the acquisition to compensate for the loss of tagging contrast (75). Although the analysis of the resulting images allows a visual assessment of the tag displacement, more advanced methods are required for quantifying the organ motion from these images. Examples include active contour methods, optical flow techniques or template matching approaches.

Phase contrast velocity encoding MRI relies on the fact that the phase accumulated is proportional to the velocity (76). Thus the values obtained at each pixel by subtracting two phase images acquired using different velocity encoding gradients will be proportional to the tissue motion (72, 73).

Pulsed field gradients methods can also be used for motion encoding being able to directly measure the tissue displacement. Two such techniques are the harmonic phase imaging (HARP) (77) and the displacement encoding via stimulated echoes (DENSE) sequence (78). The first was initially proposed for analyzing the tagging images and allows the acquisition of high-resolution data. DENSE was first used to estimate motion from the phase data. Subsequently, a strain-encoded (SENC) sequence (79) was developed to derive the strain information from the magnitude images.

In the context of PET/MRI, tagged-MRI was first suggested for tracking the respiratory motion in the abdomen and proof-of-principle studies were performed in phantoms and animals (80, 81). CSPAMM was used for tagging while the motion fields were estimated using regularized HARP (80). A single value of the regularization parameter was shown in simulations to provide accurate estimates of the motion fields at low and high noise levels (Figure 3). Alternatively, a B-spline non-rigid image registration algorithm can be used (81). However, scaling up to humans proved more difficult because of the fading of the tag lines (particularly in the liver). Instead, a navigated single-slice steady-state free precession (TrueFISP) MRI sequence was used to track the respiratory motion on the whole-body Siemens Biograph mMR scanner (82).

Generalized reconstruction by inversion of coupled systems (GRICS) (83) was proposed to obtain the respiratory motion model (and the corresponding motion corrected MR image) from the MR data acquired with a conventional sequence (84).

The feasibility of performing cardiac tagging on an integrated PET/MR scanner was also demonstrated using a cardiac beating phantom (85). Again a SPAMM sequence was used for tagging the myocardium and non-rigid B-spline registration algorithm (86) for estimating the motion fields in all three directions from the tagged MRI volumes. On the other hand, tagging might not be the optimal method when imaging the coronary arteries. Instead, it was recently suggested that the motion of these vessels could be estimated using fat-MRI (87). Even more challenging is to use tagging for estimating the motion of the lung tissue given its reduced SNR in MRI. In fact, in some of the methods already discussed, lung tissue was either masked out to avoid introducing bias in the adjacent regions (80) or the lung motion fields were interpolated from those estimated at the boundaries (48).

MRI can also be used for detecting non-rigid bulk motion (e.g. caused by the subject's repositioning on the table). For this task, a 3D high-resolution radial phase encoding (RPE) scheme can be used to reconstruct MR images with different temporal resolutions from the same data. From the high temporal resolution images, the times when bulk motion occurred can be detected so that the acquired data can be grouped into multiple bulk motion states. Next, the corresponding MR images are reconstructed and the non-rigid body motion between the various states is estimated. Finally, this information can be used to generate motion-corrected MR (and PET) images (88).

Joint estimation approaches

An interesting opportunity in the case of simultaneous PET and MRI data acquisition is to use the information derived from both modalities to estimate the motion (89). In principle,

the same deformation fields should be derived from both datasets. However, this is not always the case since the information provided by each modality is different. A registration functional was proposed to address this problem but instead of applying it to each dataset independently, the two functionals were combined into one. In this way, the influence of the PET data can be seen as a regularizer whose influence can be adjusted by modifying a single parameter, which is used in addition to a hyperelastic regularizer that penalizes changes in volume, area, and length. A preliminary evaluation of this method was performed in a simulated phantom and demonstrated improvements in the heart, lung and focal lesions (89).

MOTION COMPENSATION OF PET DATA

Pre-reconstruction techniques

This class of methods has been more widely used for rigid-body head motion correction (90), including MR-assisted motion correction in an integrated PET/MRI scanner (91). However, the respiration-related motion of several organs in the body can be approximated using rigid body parameters. For example, as already discussed, the heart can be assumed to move rigidly with the respiration and a method to account for this motion before reconstruction was proposed (92). The line-of-response corresponding to each event is first spatially transformed and then assigned to a new line-of-response using nearest neighbor interpolation. In other words, an event detected in a pair of crystals is assigned to a different pair of crystals based on the transformation matrix derived from the three rotations and three translations that define the rigid-body motion. The corrections for variable detector efficiencies and attenuation have to be performed in the line-of-response space before the reconstruction.

Reconstruction techniques

A more elegant method for using the detailed motion field is to incorporate it in the reconstruction so that all the recorded counts can be used to reconstruct an image of the organ of interest "frozen" in the chosen position. This is accomplished by modifying the PET system matrix (that relates the actual activity distribution to the measured data) to account for the non-rigid change in the activity distribution (68). The biggest advantage of this class of methods is that the counting statistics are significantly improved when compared to the standard gating techniques since no events are discarded. Furthermore, the Poisson nature of the data is maintained after correction as opposed to the post-reconstruction techniques.

The motion field can be incorporated in the list-mode maximum likelihood (MLEM) reconstruction algorithm (80). The "moved" system matrix is obtained by combining the original system matrix with the motion-warping operator, which is computed from the estimated motion field by linear interpolation. Similarly, the motion field can be incorporated in the system matrix of a list-mode ordered-subsets expectation maximization (OSEM) algorithm (81). The static MR coils (e.g. head & neck, spine arrays, etc.) attenuation and sensitivity corrections can also be integrated in the system matrix. To account for the motion-dependent subject attenuation, the attenuation map corresponding to the reference frame is deformed to match every motion frame and included in the "moved"

system matrix. Representative motion-corrected images obtained using this approach in a non-human primate are shown in Figure 4. Additionally, the scanner point spread function can also be included in the motion-dependent system matrix (82).

Given the close relationship between image reconstruction and motion estimation, it was suggested that these two steps could be performed simultaneously (93, 94). The advantages of this class of methods are that the motion blur in the gated frames is reduced and the SNR in the data used for estimating the motion is increased.

Post-reconstruction techniques

Finally, the motion fields can be used to warp the reconstructed images corresponding to each of the gates to a common reference frame. The final image is obtained by simply summing all these individual images. This simple approach was used in some of the early studies in which PET-derived motion fields were applied to the each of the gated frames (57) but also in the recent studies performed on the integrated PET/MR scanner using MR-derived motion fields (69). A representative image highlighting the improvements in image quality (e.g. improved contrast, reduced noise) after motion correction is shown in Figure 5.

WORKFLOW AND USABILITY IN CLINICAL PRACTICE

In principle, all the techniques discussed in the previous sections for controlling and characterizing the motion of internal organs can be used in an integrated PET/MR scanner. Although the main focus of most of the approaches proposed for PET/CT studies was on minimizing the emission-attenuation mismatch, it is likely that a further reduction of motion-related blurring and an increase in contrast can be achieved in integrated PET/MR scanners.

Not surprisingly, virtually all the studies in which motion control or correction was performed showed a substantial improvement in lesion delineation and uptake quantification when comparing the motion corrected to the uncorrected data. Using all the recorded events to generate the final image is desired given the SNR increase when compared to single gate reconstructions. Furthermore, the motion-compensated reconstruction algorithms provide additional benefits over the post-reconstruction methods. For example, the former result in lower variance for maximum-likelihood reconstruction and they also outperform the latter when using penalized-likelihood reconstruction up to a certain degree of smoothing (95). These results were also confirmed by an analysis of the theoretical noise properties of some of these methods using an analytical approach (96).

Ideally, very high temporal and spatial resolution motion information should be derived from the free-breathing data acquired for clinical purposes and matching motion-corrected PET and MR images should be generated automatically shortly after the examination. However, substantial progress is required in the PET/MR field to achieve such an optimistic goal. To drive future developments, new methods have to be tested in realistic situations so that the clinical utility of motion correction can be demonstrated. It is likely that a distinction will have to be made between research and clinical PET/MRI studies. In a research setting, it might be possible to use the most advanced methods to acquire the data,

the most sophisticated post-processing algorithms to derive the motion fields from these data and to integrate this information in the PET image reconstruction. Unfortunately, the data collected with many of the advanced MR techniques (e.g. tagged MRI) cannot be used for clinical diagnosis. Furthermore, in a clinical setting the data have to be acquired fast, with no additional equipment, patient preparation and operator training so that the routine clinical protocol is minimally modified. Furthermore, the cost associated with these examinations should be minimized, which is particularly difficult in the case of PET/MRI.

Although in the near feature motion control and gating approaches will continue to be used in integrated PET/MRI scanners, the field will likely move more towards data-driven approaches (42). Given the lack of ionizing radiation exposure in MR as compared to CT, an interesting opportunity in an integrated PET/MR scanner is to cross-validate the various techniques that have previously been proposed for PET- and MR-based motion characterization. Real-size phantoms capable of simulating respiratory and cardiac motion (97) will be invaluable for this task given the fact that obtaining motion-free data in human studies is impossible and a gold standard for motion characterization is not available. Subsequently, the respiratory-related motion could be estimated from one modality and the cardiac-related motion from the other modality. Alternatively, the information derived from one could be used for quality assurance and control for the other one.

A combination of these approaches and likely future developments will have to provide the right balance between accuracy, robustness, usability and cost-effectiveness before motion correction finds widespread clinical use for whole-body applications.

References

1. Rahmim A, Rousset O, Zaidi H. Strategies for Motion Tracking and Correction in PET. PET Clin. 2007; 2:251–266.

2. Drzezga A, Souvatzoglou M, Eiber M, et al. First clinical experience with integrated whole-body PET/MR: comparison to PET/CT in patients with oncologic diagnoses. J Nucl Med. 2012; 53:845–855. [PubMed: 22534830]

3. Levin C, Glover G, Deller T, et al. Prototype time-of-flight PET ring integrated with a 3T MRI system for simultaneous whole-body PET/MR imaging. J Nucl Med. 2013; 54:148.

4. Catana C, Guimaraes AR, Rosen BR. PET and MR Imaging: The Odd Couple or a Match Made in Heaven? J Nucl Med. 2013; 54:815–824. [PubMed: 23492887]

5. Townsend DW, Carney JP, Yap JT, et al. PET/CT today and tomorrow. J Nucl Med. 2004; 45 (Suppl 1):4S–14S. [PubMed: 14736831]

6. Kinahan PE, Townsend DW, Beyer T, et al. Attenuation correction for a combined 3D PET/CT scanner. Med Phys. 1998; 25:2046–2053. [PubMed: 9800714]

7. Wade OL. Movements of the thoracic cage and diaphragm in respiration. J Physiol (Lond). 1954; 124:193–212. [PubMed: 13175123]

8. Allen AM, Siracuse KM, Hayman JA, et al. Evaluation of the influence of breathing on the movement and modeling of lung tumors. Int J Radiat Oncol Biol Phys. 2004; 58:1251–1257. [PubMed: 15001270]

9. Mageras GS, Pevsner A, Yorke ED, et al. Measurement of lung tumor motion using respiration-correlated CT. Int J Radiat Oncol Biol Phys. 2004; 60:933–941. [PubMed: 15465212]

10. McLeish K, Hill DL, Atkinson D, et al. A study of the motion and deformation of the heart due to respiration. IEEE Trans Med Imaging. 2002; 21:1142–1150. [PubMed: 12564882]
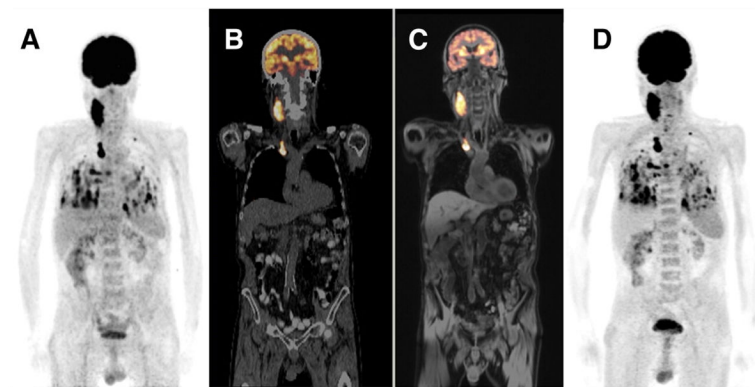
11. Wang Y, Riederer SJ, Ehman RL. Respiratory Motion of the Heart: Kinematics and the Implications for the Spatial Resolution in Coronary Imaging. Magn Reson Med. 1995; 33:713–719. [PubMed: 7596276]

12. Scott AD, Keegan J, Firmin DN. Motion in Cardiovascular MR Imaging. Radiology. 2009; 250:331–351. [PubMed: 19188310]

13. Raper AJ, Richardson DW, Kontos HA, et al. Circulatory responses to breath holding in man. J Appl Physiol. 1967; 22:201–206. [PubMed: 6018570]

14. Suramo I, Paivansalo M, Myllyla V. Cranio-caudal movements of the liver, pancreas and kidneys in respiration. Acta Radiologica-Diagnosis. 1984; 25:129–131. [PubMed: 6731017]

15. Korin HW, Ehman RL, Riederer SJ, et al. Respiratory kinematics of the upper abdominal organs - a quantitative study. Magn Reson Med. 1992; 23:172–178. [PubMed: 1531152]

16. Clifford MA, Banovac F, Levy E, et al. Assessment of hepatic motion secondary to respiration for computer assisted interventions. Comput Aided Surg. 2002; 7:291–299. [PubMed: 12582982]

17. Shimizu S, Shirato H, Aoyama H, et al. High-speed magnetic resonance imaging for four-dimensional treatment planning of conformal radiotherapy of moving body tumors. Int J Radiat Oncol Biol Phys. 2000; 48:471–474. [PubMed: 10974464]

18. Rohlfing T, Maurer CR, O'Dell WG, et al. Modeling liver motion and deformation during the respiratory cycle using intensity-based nonrigid registration of gated MR images. Med Phys. 2004; 31:427–432. [PubMed: 15070239]

19. Brandner ED, Wu A, Chen H, et al. Abdominal organ motion measured using 4D CT. Int J Radiat Oncol Biol Phys. 2006; 65:554–560. [PubMed: 16690437]

20. Feng M, Balter JM, Normolle D, et al. Characterization of Pancreatic Tumor Motion Using Cine MRI: Surrogates for Tumor Position Should Be Used With Caution. Int J Radiat Oncol Biol Phys. 2009; 74:884–891. [PubMed: 19395190]

21. Mori S, Hara R, Yanagi T, et al. Four-dimensional measurement of intrafractional respiratory motion of pancreatic tumors using a 256 multi-slice CT scanner. Radiother Oncol. 2009; 92:231–237. [PubMed: 19211167]

22. Yamashita H, Yamashita M, Futaguchi M, et al. Individually wide range of renal motion evaluated by four-dimensional computed tomography. SpringerPlus. 2014; 3:131. [PubMed: 24711985]

23. Siva S, Pham D, Gill S, et al. An analysis of respiratory induced kidney motion on four-dimensional computed tomography and its implications for stereotactic kidney radiotherapy. Radiat Oncol. 2013; 8:248. [PubMed: 24160868]

24. Pai Panandiker AS, Sharma S, Naik MH, et al. Novel assessment of renal motion in children as measured via four-dimensional computed tomography. Int J Radiat Oncol Biol Phys. 2012; 82:1771–1776. [PubMed: 21621338]

25. Dinkel J, Thieke C, Plathow C, et al. Respiratory-induced prostate motion: characterization and quantification in dynamic MRI. Strahlenther Onkol. 2011; 187:426–432. [PubMed: 21713396]

26. Sengupta PP, Korinek J, Belohlavek M, et al. Left ventricular structure and function: basic science for cardiac imaging. J Am Coll Cardiol. 2006; 48:1988–2001. [PubMed: 17112989]

27. Petitjean C, Rougon N, Cluzel P. Assessment of myocardial function: a review of quantification methods and results using tagged MRI. J Cardiovasc Magn Reson. 2005; 7:501–516. [PubMed: 15881535]

28. Seppenwoolde Y, Shirato H, Kitamura K, et al. Precise and real-time measurement of 3D tumor motion in lung due to breathing and heartbeat, measured during radiotherapy. Int J Radiat Oncol Biol Phys. 2002; 53:822–834. [PubMed: 12095547]

29. Palmer J, Yang J, Pan T, et al. Motion of the esophagus due to cardiac motion. PLoS ONE. 2014; 9:e89126. [PubMed: 24586540]

30. Chung S, Kim K-E, Park M-S, et al. Liver stiffness assessment with tagged MRI of cardiac-induced liver motion in cirrhosis patients. J Magn Reson Imaging. 2014; 39:1301–1307. [PubMed: 24719241]

31. Bradley JA, Paulson ES, Ahunbay E, et al. Dynamic MRI Analysis of Tumor and Organ Motion During Rest and Deglutition and Margin Assessment for Radiotherapy of Head-and-Neck Cancer. Int J Radiat Oncol Biol Phys. 2011; 81:e803–e812. [PubMed: 21300480]

32. Padhani AR, Khoo VS, Suckling J, et al. Evaluating the effect of rectal distension and rectal movement on prostate gland position using cine MRI. Int J Radiat Oncol Biol Phys. 1999; 44:525–533. [PubMed: 10348281]

33. Langen KM, Willoughby TR, Meeks SL, et al. Observations on Real-Time Prostate Gland Motion Using Electromagnetic Tracking. Int J Radiat Oncol Biol Phys. 2008; 71:1084–1090. [PubMed: 18280057]

34. Tsai C-L, Wu J-K, Wang C-W, et al. Using Cone-Beam Computed Tomography to Evaluate the Impact of Bladder Filling Status on Target Position in Prostate Radiotherapy. Strahlenther Onkol. 2009; 185:588–595. [PubMed: 19756425]

35. van Heeswijk RB, Bonanno G, Coppo S, et al. Motion Compensation Strategies in Magnetic Resonance Imaging. Crit Rev Biomed Eng. 2012; 40:99–119. [PubMed: 22668237]

36. McClelland JR, Hawkes DJ, Schaeffter T, et al. Respiratory motion models: A review. Med Image Anal. 2013; 17:19–42. [PubMed: 23123330]

37. Nehmeh SA, Erdi YE. Respiratory motion in positron emission tomography/computed tomography: a review. Semin Nucl Med. 2008; 38:167–176. [PubMed: 18396177]

38. Pepin A, Daouk J, Bailly P, et al. Management of respiratory motion in PET/computed tomography: the state of the art. Nucl Med Commun. 2014; 35:113–122. [PubMed: 24352107]

39. Visvikis, D.; Barret, O.; Fryer, T., et al. A posteriori respiratory motion gating of dynamic PET images. In: Metzler, SD., editor. IEEE Nucl Sc Symp Conf Rec. New York: IEEE; 2004. p. 3276-3280.

40. Schleyer PJ, O'Doherty MJ, Barrington SF, et al. Retrospective data-driven respiratory gating for PET/CT. Phys Med Biol. 2009; 54:1935–1950. [PubMed: 19265207]

41. Schleyer PJ, O'Doherty MJ, Marsden PK. Extension of a data-driven gating technique to 3D, whole body PET studies. Phys Med Biol. 2011; 56:3953–3965. [PubMed: 21666288]

42. Kesner AL, Schleyer PJ, Büther F, et al. On transcending the impasse of respiratory motion correction applications in routine clinical imaging–a consideration of a fully automated data driven motion control framework. EJNMMI Physics. 2014; 1:8.

43. Dawood M, Buther F, Lang N, et al. Respiratory gating in positron emission tomography: a quantitative comparison of different gating schemes. Med Phys. 2007; 34:3067–3076. [PubMed: 17822014]

44. Nehmeh SA, Erdi YE, Meirelles GS, et al. Deep-inspiration breath-hold PET/CT of the thorax. J Nucl Med. 2007; 48:22–26. [PubMed: 17204695]

45. Holland AE, Goldfarb JW, Edelman RR. Diaphragmatic and cardiac motion during suspended breathing: preliminary experience and implications for breath-hold MR imaging. Radiology. 1998; 209:483–489. [PubMed: 9807578]

46. Ehman RL, Felmlee JP. Adaptive technique for high-definition MR imaging of moving structures. Radiology. 1989; 173:255–263. [PubMed: 2781017]

47. McConnell MV, Khasgiwala VC, Savord BJ, et al. Prospective adaptive navigator correction for breath-hold MR coronary angiography. Magn Reson Med. 1997; 37:148–152. [PubMed: 8978644]

48. King AP, Buerger C, Tsoumpas C, et al. Thoracic respiratory motion estimation from MRI using a statistical model and a 2-D image navigator. Med Image Anal. 2012; 16:252–264. [PubMed: 21959365]

49. Uribe S, Muthurangu V, Boubertakh R, et al. Whole-heart cine MRI using real-time respiratory self-gating. Magn Reson Med. 2007; 57:606–613. [PubMed: 17326164]

50. Lenz GW, Haacke EM, White RD. Retrospective cardiac gating: A review of technical aspects and future directions. Magn Reson Imaging. 1989; 7:445–455. [PubMed: 2607896]

51. Leiner T, Katsimaglis G, Yeh EN, et al. Correction for heart rate variability improves coronary magnetic resonance angiography. J Magn Reson Imaging. 2005; 22:577–582. [PubMed: 16142699]

52. Roes SD, Korosoglou G, Schar M, et al. Correction for heart rate variability during 3D whole heart MR coronary angiography. J Magn Reson Imaging. 2008; 27:1046–1053. [PubMed: 18425831]

53. Gupta A, Weeks AR, Richie SM. Simulation of elevated T-waves of an ECG inside a static magnetic field (MRI). IEEE Trans Biomed Eng. 2008; 55:1890–1896. [PubMed: 18595808]
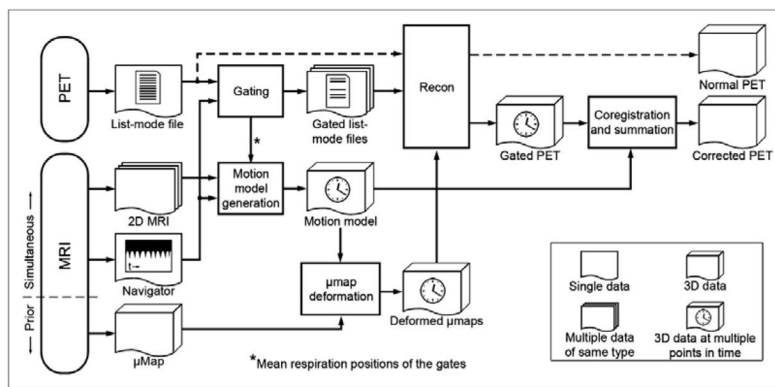
54. Fischer SE, Wickline SA, Lorenz CH. Novel real-time R-wave detection algorithm based on the vectorcardiogram for accurate gated magnetic resonance acquisitions. Magn Reson Med. 1999; 42:361–370. [PubMed: 10440961]

55. Larson AC, White RD, Laub G, et al. Self-gated cardiac cine MRI. Magn Reson Med. 2004; 51:93–102. [PubMed: 14705049]

56. Crowe ME, Larson AC, Zhang Q, et al. Automated rectilinear self-gated cardiac cine imaging. Magn Reson Med. 2004; 52:782–788. [PubMed: 15389958]

57. Lamare F, Le Maitre A, Dawood M, et al. Evaluation of respiratory and cardiac motion correction schemes in dual gated PET/CT cardiac imaging. Med Phys. 2014; 41:072504-072501–072504-072513. [PubMed: 24989407]

58. Henningsson M, Botnar R. Advanced Respiratory Motion Compensation for Coronary MR Angiography. Sensors. 2013; 13:6882–6899. [PubMed: 23708271]

59. Koivumaki T, Nekolla SG, Furst S, et al. An integrated bioimpedance-ECG gating technique for respiratory and cardiac motion compensation in cardiac PET. Phys Med Biol. 2014; 59:6373–6385. [PubMed: 25295531]

60. Pipe JG. Motion correction with PROPELLER MRI: Application to head motion and free-breathing cardiac imaging. Magn Reson Med. 1999; 42:963–969. [PubMed: 10542356]

61. Wang CC, Huang TY. Self-gated PROPELLER-encoded cine cardiac imaging. Int J Cardiovasc Imaging. 2012; 28:1477–1485. [PubMed: 22042429]

62. Dawood M, Buther F, Jiang X, et al. Respiratory motion correction in 3-D PET data with advanced optical flow algorithms. IEEE Trans Med Imaging. 2008; 27:1164–1175. [PubMed: 18672433]

63. Gilland DR, Mair BA, Parker JG. Motion estimation for cardiac emission tomography by optical flow methods. Phys Med Biol. 2008; 53:2991–3006. [PubMed: 18475004]

64. Klein GJ, Reutter BW, Huesman RH. Non-rigid summing of gated PET via optical flow. IEEE Trans Nucl Sci. 1997; 44:1509–1512.

65. Dawood M, Gigengack F, Jiang XY, et al. A mass conservation-based optical flow method for cardiac motion correction in 3D-PET. Med Phys. 2013; 40:9.

66. Gigengack F, Ruthotto L, Burger M, et al. Motion correction in dual gated cardiac PET using mass-preserving image registration. IEEE Trans Med Imaging. 2012; 31:698–712. [PubMed: 22084048]

67. Bai W, Brady M. Regularized B-spline deformable registration for respiratory motion correction in PET images. Phys Med Biol. 2009; 54:2719–2736. [PubMed: 19351979]

68. Lamare F, Ledesma Carbayo MJ, Cresson T, et al. List-mode-based reconstruction for respiratory motion correction in PET using non-rigid body transformations. Phys Med Biol. 2007; 52:5187–5204. [PubMed: 17762080]

69. Wurslin C, Schmidt H, Martirosian P, et al. Respiratory Motion Correction in Oncologic PET Using T1-Weighted MR Imaging on a Simultaneous Whole-Body PET/MR System. J Nucl Med. 2013; 54:464–471. [PubMed: 23287577]

70. Grimm, R.; Furst, S.; Dregely, I., et al. Self-gated Radial MRI for Respiratory Motion Compensation on Hybrid PET/MR Systems. In: Mori, K.; Sakuma, I.; Sato, Y.; Barillot, C.; Navab, N., editors. Medical Image Computing and Computer-Assisted Intervention. Vol. 8151. Berlin: Springer-Verlag Berlin; 2013. p. 17-24.

71. Ozturk C, Derbyshire JA, McVeigh ER. Estimating motion from MRI data. Proc IEEE. 2003; 91:1627–1648.

72. Zerhouni EA, Parish DM, Rogers WJ, et al. Human-heart-tagging with MR imaging - A method for noninvasive assessment of myocardial motion. Radiology. 1988; 169:59–63. [PubMed: 3420283]

73. Axel L, Dougherty L. MR imaging of motion with spatial modulation of magnetization. Radiology. 1989; 171:841–845. [PubMed: 2717762]

74. Mosher TJ, Smith MB. A DANTE tagging sequence for the evaluation of translational sample motion. Magn Reson Med. 1990; 15:334–339. [PubMed: 2392056]

75. Fischer SE, McKinnon GC, Maier SE, et al. Improved myocardial tagging contrast. Magn Reson Med. 1993; 30:191–200. [PubMed: 8366800]
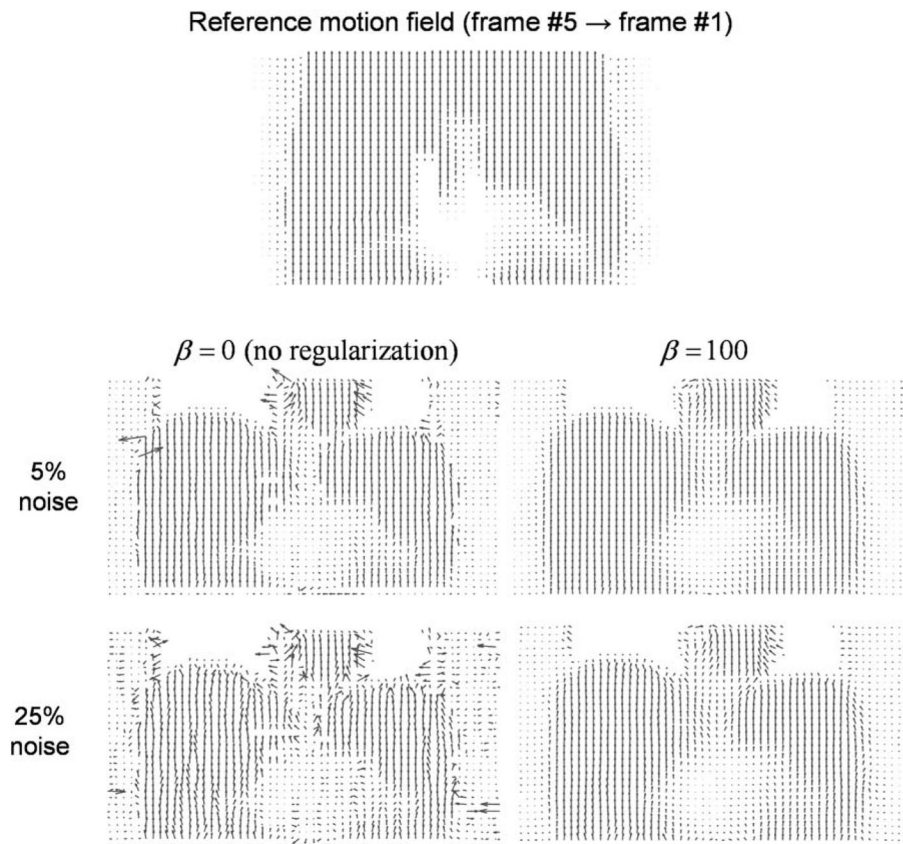
76. Moran PR. A flow velocity zeugmatographic interlace for NMR imaging in humans. Magn Reson Imaging. 1982; 1:197–204. [PubMed: 6927206]

77. Osman NF, McVeigh ER, Prince JL. Imaging heart motion using harmonic phase MRI. IEEE Trans Med Imaging. 2000; 19:186–202. [PubMed: 10875703]

78. Aletras AH, Ding SJ, Balaban RS, et al. DENSE: Displacement encoding with stimulated echoes in cardiac functional MRI. J Magn Reson. 1999; 137:247–252. [PubMed: 10053155]

79. Osman NF, Sampath S, Atalar E, et al. Imaging longitudinal cardiac strain on short-axis images using strain-encoded MRI. Magn Reson Med. 2001; 46:324–334. [PubMed: 11477637]

80. Guerin B, Cho S, Chun SY, et al. Nonrigid PET motion compensation in the lower abdomen using simultaneous tagged-MRI and PET imaging. Med Phys. 2011; 38:3025–3038. [PubMed: 21815376]

81. Chun SY, Reese TG, Ouyang JS, et al. MRI-Based Nonrigid Motion Correction in Simultaneous PET/MRI. J Nucl Med. 2012; 53:1284–1291. [PubMed: 22743250]

82. Petibon Y, Huang C, Ouyang J, et al. Relative role of motion and PSF compensation in whole-body oncologic PET-MR imaging. Med Phys. 2014; 41:042503. [PubMed: 24694156]

83. Odille F, Vuissoz PA, Marie PY, et al. Generalized reconstruction by inversion of coupled systems (GRICS) applied to free-breathing MRI. Magn Reson Med. 2008; 60:146–157. [PubMed: 18581355]

84. Fayad, HJ.; Odille, F.; Felblinger, J., et al. A generic PET/MRI respiratory motion correction using a generalized reconstruction by inversion of coupled systems (GRICS) approach. Paper presented at: IEEE Nucl Sci Symp Conf Rec; 2012.

85. Petibon Y, Ouyang J, Zhu X, et al. Cardiac motion compensation and resolution modeling in simultaneous PET-MR: a cardiac lesion detection study. Phys Med Biol. 2013; 58:2085. [PubMed: 23470288]

86. Ledesma-Carbayo MJ, Derbyshire JA, Sampath S, et al. Unsupervised estimation of myocardial displacement from tagged MR sequences using nonrigid registration. Magn Reson Med. 2008; 59:181–189. [PubMed: 18058938]

87. Petibon Y, El Fakhri G, Nezafat R, et al. Towards coronary plaque imaging using simultaneous PET-MR: a simulation study. Phys Med Biol. 2014; 59:1203–1222. [PubMed: 24556608]

88. Kolbitsch C, Prieto C, Tsoumpas C, et al. A 3D MR-acquisition scheme for nonrigid bulk motion correction in simultaneous PET-MR. Med Phys. 2014; 41:082304. [PubMed: 25086553]

89. Fieseler M, Gigengack F, Jiang X, et al. Motion correction of whole-body PET data with a joint PET-MRI registration functional. Biomed Eng Online. 2014; 13 (Suppl 1):S2. [PubMed: 25077815]

90. Bloomfield PM, Spinks TJ, Reed J, et al. The design and implementation of a motion correction scheme for neurological PET. Phys Med Biol. 2003; 48:959–978. [PubMed: 12741495]

91. Catana C, Benner T, van der Kouwe A, et al. MRI-assisted PET motion correction for neurologic studies in an integrated MR-PET scanner. J Nucl Med. 2011; 52:154–161. [PubMed: 21189415]

92. Livieratos L, Stegger L, Bloomfield PM, et al. Rigid-body transformation of list-mode projection data for respiratory motion correction in cardiac PET. Phys Med Biol. 2005; 50:3313–3322. [PubMed: 16177511]

93. Gilland DR, Mair BA, Bowsher JE, et al. Simultaneous reconstruction and motion estimation for gated cardiac ECT. IEEE Trans Nucl Sci. 2002; 49:2344–2349.

94. Blume M, Martinez-Moller A, Keil A, et al. Joint Reconstruction of Image and Motion in Gated Positron Emission Tomography. IEEE Trans Med Imaging. 2010; 29:1892–1906. [PubMed: 20562034]

95. Asma E, Manjeshwar R, Thielemans K, et al. Theoretical Comparison of Motion Correction Techniques for PET Image Reconstruction. IEEE Nucl Sc Symp Conf Rec. 2006; 1–6:1762–1767.

96. Chun SY, Fessler JA. Noise Properties of Motion-Compensated Tomographic Image Reconstruction Methods. IEEE Trans Med Imaging. 2013; 32:141–152. [PubMed: 22759442]

97. Fieseler M, Kugel H, Gigengack F, et al. A dynamic thorax phantom for the assessment of cardiac and respiratory motion correction in PET/MRI: A preliminary evaluation. Nucl Instrum Methods Phys Res Sect A-Accel Spectrom Dect Assoc Equip. 2013; 702:59–63.
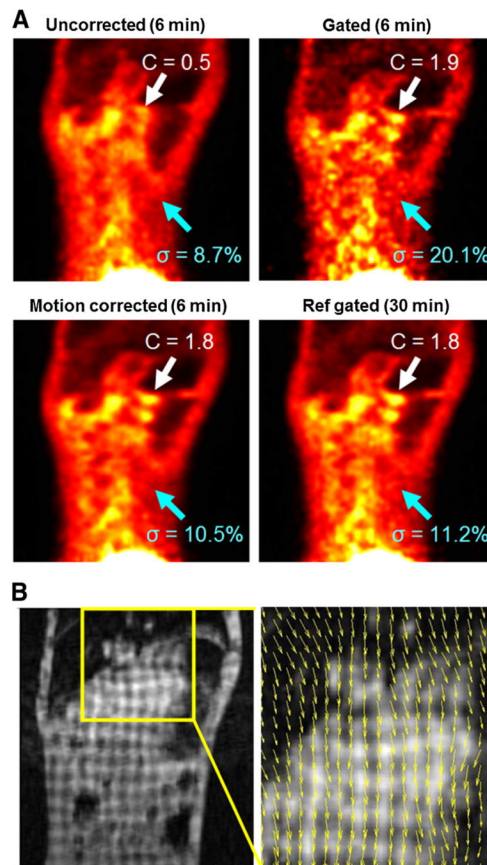
Figure 1.
Proof-of-principle whole-body PET/MRI study in a patient with metastasized thyroid cancer. The PET/CT and PET/MRI exams were performed sequentially on the same day. The ^{18}F-FDG PET acquired on the PET/CT scanner is displayed as a maximum-intensity projection (A) and overlaid (in orange) on the corresponding low-dose CT image (B). The ^{18}F-FDG PET acquired on the PET/MRI scanner is shown overlaid (in orange) on the corresponding water-weighted Dixon MR image (C) and displayed as a maximum-intensity projection (D). This research was originally published in JNM (2). © by the Society of Nuclear Medicine and Molecular Imaging, Inc.
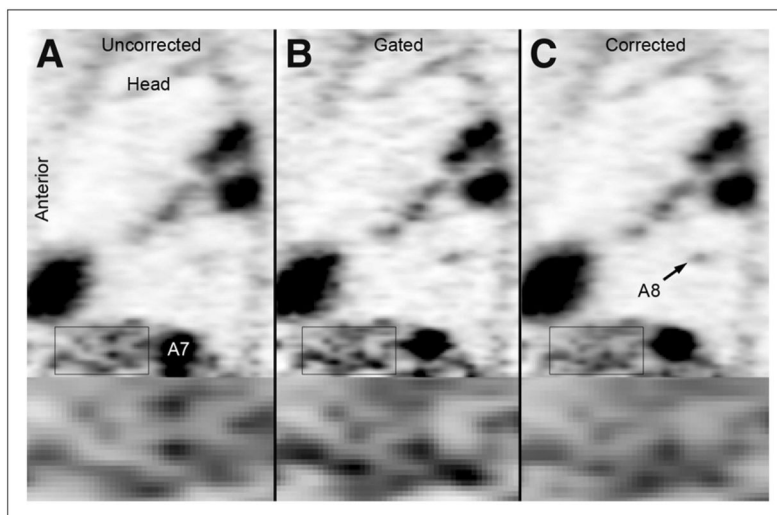
Figure 2.
Overview of a potential workflow for data acquisition, motion estimation and PET motion correction in an integrated PET/MRI scanner. The dashed line represents the standard PET data processing, while the solid lines show the data flow with motion correction. This research was originally published in JNM (69). © by the Society of Nuclear Medicine and Molecular Imaging, Inc.

Figure 3.
Motion estimation using regularized HARP. The reference motion field (upper row) as well as those derived from the tagged MRI data simulated at two noise levels with and without regularization (lower rows) are shown. This research was originally published in Medical Physics (80).

Figure 4.
Proof-of-principle MR-based motion compensation in the reconstruction in a free-breathing non-human primate. (A) The contrast in the motion corrected and gated images is significantly increased compared with the uncorrected image. The noise in the motion corrected image is reduced compared to the gated image. The quality of the motion corrected image is similar to that of the five-times longer gated acquisition. (B) Corresponding tagged MR image and the estimated motion field during inspiration. This research was originally published in JNM (81). © by the Society of Nuclear Medicine and Molecular Imaging, Inc.

Figure 5.
Proof-of-principle MR-based motion compensation post-reconstruction in a cancer patient. The uncorrected (A), gated (B), and corrected (C) sagittal PET images demonstrating multiple FDG avid lesions in the spleen (A7) and lung (A8) are shown. The lesion in the spleen is significantly smaller in the gated and corrected images. The lung metastasis (A8) is only observed in the gated and corrected images. The noise is increased in the gated images (see zoomed regions). This research was originally published in JNM (69). © by the Society of Nuclear Medicine and Molecular Imaging, Inc.